J. Fluid Mech. (2006), *vol.* 552, *pp.* 353–380.
doi:10.1017/S0022112006008688 Printed in the United Kingdom

Bubble friction drag reduction in a high-Reynolds-number flat-plate turbulent boundary layer

By WENDY C. SANDERS, ERIC S. WINKEL, DAVID R. DOWLING, MARC PERLIN AND STEVEN L. CECCIO

Department of Mechanical Engineering, University of Michigan, Ann Arbor, MI 48109, USA

(Received 6 February 2004 and in revised form 14 October 2005)

Turbulent boundary layer skin friction in liquid flows may be reduced when bubbles are present near the surface on which the boundary layer forms. Prior experimental studies of this phenomenon reached downstream-distance-based Reynolds numbers (Re_x) of several million, but potential applications may occur at Re_x orders of magnitude higher. This paper presents results for Re_x as high as 210 million from skin-friction drag-reduction experiments conducted in the USA Navy's William B. Morgan Large Cavitation Channel (LCC). Here, a near-zero-pressure-gradient flat-plate turbulent boundary layer was generated on a 12.9 m long hydraulically smooth flat plate that spanned the 3 m wide test section. The test surface faced downward and air was injected at volumetric rates as high as $0.38\,\mathrm{m^3\,s^{-1}}$ through one of two flush-mounted 40 μm sintered-metal strips that nearly spanned the test model at upstream and downstream locations. Spatially and temporally averaged shear stress and bubble-image-based measurements are reported here for nominal test speeds of 6, 12 and $18\,\mathrm{m\,s^{-1}}$. The mean bubble diameter was ∼300 μm. At the lowest test speed and highest air injection rate, buoyancy pushed the air bubbles to the plate surface where they coalesced to form a nearly continuous gas film that persisted to the end of the plate with near-100 % skin-friction drag reduction. At the higher two flow speeds, the bubbles generally remained distinct and skin-friction drag reduction was observed when the bubbly mixture was closer to the plate surface than 300 wall units of the boundary-layer flow without air injection, even when the bubble diameter was more than 100 of these wall units. Skin-friction drag reduction was lost when the near-wall shear induced the bubbles to migrate from the plate surface. This bubble-migration phenomenon limited the persistence of bubble-induced skin-friction drag reduction to the first few metres downstream of the air injector in the current experiments.

1. Introduction

1.1. *Background and motivation*

Both passive and active means to reduce the skin-friction of a fluid flowing near a solid surface are of interest in a variety of marine, hydraulic and aerospace applications. Fully passive friction-reduction methods that function without ongoing expenditure of energy include applying riblets to the surface, adding compliance to the surface, and shaping and polishing the surface to maintain laminar flow to the greatest possible downstream extent. Fully active skin-friction control methods involving unsteady

energy addition include transverse wall oscillations and electro-kinetic forcing of the near-wall flow. Between fully-passive and -active approaches lie three techniques that involve a quasi-steady energy expenditure at constant speed to achieve skin friction reduction: suction (or blowing) through the surface; injection of a polymeric solution from the surface; and injection of gas or bubbles from the surface. This final technique, hereinafter referred to as BDR (bubble-induced skin-friction drag reduction), is the subject of this paper.

Prior BDR experiments (reviewed in Merkle & Deutsch 1992) have shown that this technique can reliably produce drag reductions of greater than 50 %, and as large as 80 % to 90 %, at downstream-distance-based Reynolds numbers (Re_x) of several million on flat plates having a length of 1 m or so. Thus, through-hull air injection is a potentially attractive and promising means to achieve drag reduction for commercial and military watercraft, provided it remains effective at much higher Reynolds numbers, $Re_x \sim 10^9$ to 10^{10}, and over much longer flow distances, tens or even hundreds of metres. This paper describes the results of a controlled experimental study conducted at Re_x values as high as 2.1×10^8 and at downstream distances in excess of 10 m that was intended to close the present Reynolds-number and length-scale gaps between BDR experiments and maritime applications. In addition, the investigation reported here sought to determine the mechanism(s) governing the downstream persistence of bubble-induced skin-friction drag reduction so that scaling of these and prior experimental results to maritime applications might be possible.

This paper is divided into five sections. The remainder of this section provides a review of prior BDR studies. Section 2 describes the current experiments and § 3 presents the main results. Section 4 presents simple scaling analyses relevant to wall-bounded bubbly shear flows and compares the present effort to prior research on passive scalar mixing in a turbulent boundary layer. The final section summarizes this investigation and presents conclusions.

A comprehensive review of the first two decades of work on BDR is provided by Merkle & Deutsch (1992); hence, the summary provided in the following paragraphs is brief and emphasizes flat-plate studies. McCormick & Bhattacharyya (1973) reported the earliest successful BDR experiments (Re_x to 1.8×10^6). About the same time, Soviet workers (Migirenko & Evseev 1974; Bogdevich & Evseev 1976; Bogdevich & Malyuga 1976) observed that the maximum level of drag reduction occurred immediately downstream of gas injection and did not persist with increasing downstream distance. Madavan, Deutsch & Merkle (1984) made BDR measurements in a zero-pressure-gradient turbulent boundary layer at Re_x as large as 10^7 and found that BDR improved with decreasing flow speed, increasing gas injection rates, and when buoyancy pushed bubbles toward the plate surface. Madavan *et al.* (1985*a*) also determined that the pore size of the air injector had little effect on BDR for pore sizes from 0.5 to 100 μm. Pal, Merkle & Deutsch (1988) found that bubbles must be within 200 wall units of the surface to produce noticeable BDR. Fontaine & Deutsch (1992) determined that BDR did not depend on the density or composition of the injected gas. Takahashi *et al.* (2001) examined BDR at Re_x as high as 25 million and found that variations in bubble size and boundary-layer thickness did not significantly influence the level of drag reduction. Kawamura *et al.* (2003) found a similar insensitivity to bubble size for bubble radii of 250 to 1000 μm at similar Re_x values. BDR studies have also involved axisymmetric bodies (Deutsch & Castano 1986; Clark & Deutsch 1991) and sea trials (Kodama *et al.* 2000).

In spite of these many fine studies, the understanding of BDR is not sufficiently advanced to predict its persistence downstream of the air injector at high Reynolds

number. The primary emphasis of this manuscript is documenting BDR persistence at high Reynolds number in a flat-plate turbulent boundary layer.

Prior dimensionless scaling of BDR has involved the skin friction coefficient, C_F,

$$C_F = \tau_w \big/ \tfrac{1}{2}\rho U^2, \tag{1.1}$$

where τ_w is the skin friction, ρ is the liquid density, and U is the local flow speed at the outer edge of the boundary layer, along with a variety of flux-based estimates of the void fraction within the boundary layer. Here, C_{Fo} will refer to skin friction measured without bubbles, and BDR results will be presented as a skin friction ratio, C_F/C_{Fo}. This ratio goes to zero when BDR is completely successful. A fractional value of BDR is commonly obtained from $1 - C_F/C_{Fo}$. In addition, the flow's friction velocity u^* is defined in the usual way: $u^* = \sqrt{\tau_w/\rho}$, with u_o^* being the friction velocity without air injection.

Several flux-based void-fraction estimates have been used in attempts to collapse skin-friction ratio measurements across gas injection rate, flow speed, boundary-layer thickness and downstream distance. Madavan *et al.* (1984) and others have plotted BDR data *vs.* Q_a/SU, where Q_a is the volumetric flow rate of air ($\mathrm{m^3\,s^{-1}}$) and S is a reference area, typically the wetted surface of the porous bubble injector, with some success. However, the appropriate reference area was clearly experiment specific. Madavan *et al.* (1985*a*) showed that BDR results collapsed better when plotted against a boundary-layer flux-based void fraction, $Q_a/(Q_a + Q_w)$ where Q_w is the volume flux of water in the boundary-layer when air is not injected, $Q_w = U(\delta_o - \delta_o^*)b$, δ_o and δ_o^* are the boundary layer's 99 % and displacement thicknesses, respectively, without air injection, and b is the cross-stream span of the experiment. Deutsch *et al.* (2003) proposed a revised void-faction estimate for BDR on rough surfaces, $(u_{R,o}^*/u_o^*)Q_a/(Q_a + U\theta_o b)$, where θ_o is the single-phase boundary-layer momentum thickness, $u_{R,o}^*$ is the single-phase friction velocity when the surface is rough, and u_o^* is the single-phase friction velocity when the surface is smooth. For hydraulically smooth surfaces, as in the current investigation, the friction velocity ratio in the revised void-fraction estimate reduces to unity.

A simultaneous strength and weakness of using these flux-based void fractions is that they only involve Q_a, parameters of the injector, and parameters of the equivalent single-phase boundary layer. These can all be measured readily or estimated from correlations. However, the characteristics of the bubbly boundary layer are not included in such void fraction estimates, and attempts to collapse BDR data from different experiments based on them have been imperfect (see § 3.2). The present situation implies that an effective scaling of BDR awaits discovery. The measurements presented here should contribute to the search for a proper scaling of BDR.

This search has also been pursued through analytical and numerical efforts to determine and understand BDR mechanisms. Madavan *et al.* (1984) considered the polymer- and/or particulate-flow hypothesis of Lumley (1973, 1977) as a means of explaining BDR. Marié (1987) explored the implications of changing the bulk density and viscosity beyond the sublayer on the mean boundary-layer velocity profile during BDR. Legner (1984) used a simple stress model that included density reduction and turbulence modification to explain some BDR observations. Madavan *et al.* (1985*b*) modelled the bubbly boundary layer as a homogeneous fluid with spatially varying density and viscosity, and found agreement with the experimental results of Madavan *et al.* (1985*a*). Hinze (1955) determined that the energy necessary for bubble splitting may be provided by turbulent fluctuations. Based on such energy exchange, Meng & Uhlman (1998) proposed bubble splitting as a mechanism for BDR.

Direct numerical simulation (DNS) of turbulent bubbly flows has been conducted in the search for mechanisms. Unfortunately, such studies are only possible at modest Reynolds numbers but have been attempted in free shear flows (Druzhinin & Elghobashi 1998), and channel flows (Xu, Maxey & Karniadakis 2002; Fernández, Lu & Tryggvason 2003; Vance *et al.* 2003), and in a turbulent boundary layer (Ferrante & Elghobashi 2004). In these studies, bubbles were found to migrate into and disrupt vortical structures. Furthermore, for the calculations that predicted BDR, the initial bubble seeding, density reduction, bubble-turbulence interactions and bubble-wall proximity were all found to be important. Thus, no simple scaling of BDR has yet emerged from these efforts.

In total, these prior studies of BDR suggest that multiple mechanisms are simultaneously at work. Although the addition of bubbles to a liquid increases its volume-averaged viscosity, the corresponding reduction in density or modification of the turbulence in a boundary layer can apparently overwhelm this effect and lead to reduced skin friction. If the density reduction was dynamically passive so that the peak Reynolds shear stress in the boundary layer remained proportional to the density, then the skin friction ratio, C_F/C_{Fo}, should nearly equal $1-\gamma_{wall}$ where γ_{wall} is the near-wall void fraction. However, bubbles can also modify the turbulent fluctuations leading to momentum transport, and it has been determined numerically that bubble-induced turbulence modification is greatest when the bubbles sizes are matched approximately to the smallest turbulence scales. For wall-bounded flows, bubbles with diameters of a few $l_{v,o}$, where $l_{v,o}$ is the viscous wall unit of the equivalent boundary layer without bubbles, are thought to most effectively modify turbulence. However, none of the prior experiments, nor the one described here, injected such small bubbles as they are difficult to produce in sufficient quantity. Instead, the smallest bubbles were typically $\sim 100\, l_{v,o}$, and BDR was observed anyway. The hypothesis that increased bubble coalescence and splitting leads to turbulence modification and subsequent BDR is plausible, but has yet to be validated experimentally. Whether both the density reduction and turbulence modification are important, all prior studies agree that the bubbles must be close to the wall or BDR is lost. Thus, inner boundary-layer parameters must be important, therefore it is not surprising that outer- or global-parameter scalings of BDR are imperfect (see § 3.2, and figures 7 and 8).

2. Experimental methods

2.1. *Flow facility and test model*

The experiments were conducted in the USA Navy's Large Cavitation Channel (LCC), the world's largest low-turbulence recirculating water tunnel (see Park, Cutbirth & Brewer 2003; Etter *et al.* 2005). Flowing water enters the LCC's test-section through a 6:1 contraction. The nominal test section dimensions are 13 m (length) by 3.05 m × 3.05 m (width and height). In the absence of a test model, test-section flow speeds and pressures can be set from 0.5 to 18.3 $\mathrm{m\,s^{-1}}$ and from 3.5 to 410 kPa, respectively. The LCC's free-stream turbulence level is below 0.5 %.

The test model, shown schematically in figure 1, was a rigid flat plate ($L = 12.9$ m long, 3.0 m wide, 18.4 cm thick) designed to span the width and run the length of the LCC's test section. Its leading edge was a 4:1 ellipse and the test surface of the model faced downward so that gravitational buoyancy forced bubbles toward the test surface. The experimental x-axis begins at the model's leading edge and increases in the downstream direction. The y-axis is normal to the test surface defined by $y = 0$, and increases into the flow. The z-axis runs spanwise, completing a right-handed coordinate system. The model was constructed in three sections that were fitted with

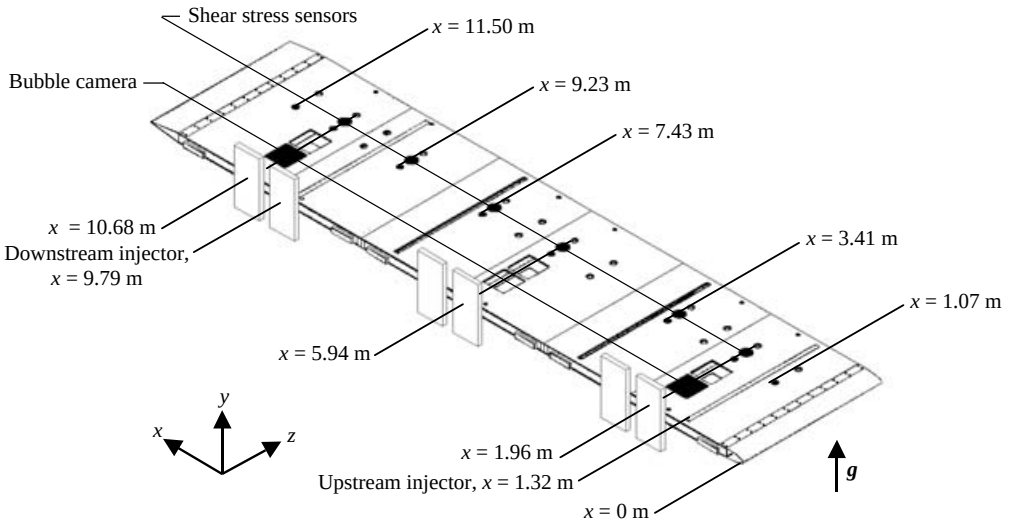

FIGURE 1. Schematic drawing of the test model. The shear stress sensors were located 50.8 cm from the centre span. The bubble camera was located 77.5 cm from the centre span. The streamwise locations of the instrumentation are indicated relative to the leading edge of the model at $x = 0$. The observation windows were centred at $x = 1.96$ m, 5.94 m, and 10.68 m. For clarity, the model is presented with the test surface facing upward. The model was oriented with the test-surface facing downward during the experiment.

precision-machined slot-and-key mechanisms to allow a repeatable and seamless assembly. It was held rigidly in place with 12 metal mounting plates that replaced LCC test-section windows. The test surface was made from 304 stainless steel and was polished while fully assembled to a root-mean-square surface roughness of $k \leqslant 0.4\,\mu$m as measured by a Mitutoyo SJ-201 surface roughness meter. A distributed roughness boundary-layer trip, consisting of a film of epoxy embedded with nominal 120 μm diameter particles arranged randomly with a separation of 2 to 5 mm, was applied from $2.5\,\text{cm} \leqslant x \leqslant 27.5\,\text{cm}$ across the entire span of the model (as recommended by Nagib 2002, personal communication). The model's trailing edge was a 15° full-angle wedge truncated with a 40° asymmetric bevel where its thickness decreased to ∼2.5 cm. The mass of the entire plate assembly was approximately 17 000 kg. The edges of the model were sealed to the LCC sidewalls with an inflatable gasket. Edge fairings (fillets) were also installed along the model-side wall junction to minimize cavitation and junction flow disturbances. These fairings were tapered to zero thickness to allow optical/visual access to the test-surface side of the model at the observation windows, shown in figure 1. The model's thickness produced a test-section area blockage of 6 %. As shown in figure 2, the model was mounted with its centreplane 5.7 cm below the test section's vertical centreline. During testing, minor pressure differences between the top and bottom of the model produced a maximum vertical displacement of 2 mm at 50 % span.

For the experiments reported here, it was not possible to measure the flow speed well upstream of the model because of its length relative to the test-section length. Thus, nominal inlet flow speeds were monitored by a single-component laser Doppler velocimeter (LDV) at the fixed location $x = -3.2$ cm, $y = 44.8$ cm and $z = 76.2$ cm from the LCC wall (25 % span); and by a two-component LDV at $x = 10.68$ m mounted on multi-axis traverse (these LDVs are described in Bourgoyne *et al.* 2003). The model

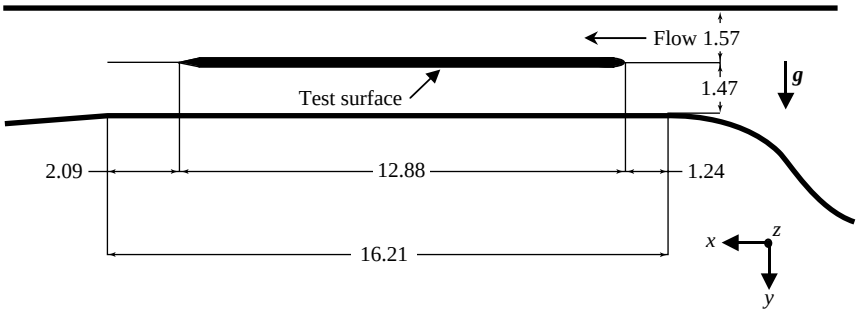

FIGURE 2. The test-section geometry and the model placement; dimensions are in metres. The diagram shows a side view looking in the spanwise direction with the test surface facing downward.

x/L	$U(\mathrm{m\,s^{-1}})$	$K'3\times10^{10}$	Re_x 3×10^6	δ_o–δ_o^* (mm)	θ_o (mm)	$l_{v,o}$ (μm)	k_o^+
	6.36	5.1	12	24	2.7	4.7	0.1
0.15	12.76	2.9	25	21	2.3	2.5	0.2
	19.21	2.2	38	19	2.2	1.7	0.2
	6.39	5.1	22	38	4.2	4.8	0.1
0.26	12.83	2.8	44	33	3.6	2.5	0.2
	19.33	2.1	66	30	3.4	1.7	0.2
	6.45	5.0	38	59	6.5	5.0	0.1
0.46	12.94	2.8	76	51	5.7	2.6	0.2
	19.53	2.1	115	47	5.2	1.8	0.2
	6.48	4.9	48	70	7.8	5.1	0.1
0.58	13.01	2.7	96	61	6.8	2.7	0.1
	19.65	2.1	144	56	6.2	1.8	0.2
	6.52	4.9	60	83	9.3	5.1	0.1
0.72	13.10	2.7	119	72	8.0	2.7	0.1
	19.80	2.0	180	67	7.4	1.8	0.2
	6.55	4.8	69	94	10.0	5.2	0.1
0.83	13.17	2.7	139	81	9.6	2.7	0.1
	19.91	2.0	209	75	9.3	1.8	0.2

TABLE 1. Single-phase free-stream velocity U; acceleration parameter, K'; Reynolds number based on downstream distance Re_x; vertical dimension of the volume of fluid flow through the boundary layer, δ_o–δ_o^*; momentum thickness, θ_o; and the viscous wall unit, $l_{v,o}$, for each of the primary streamwise measurement locations. The dimensionless surface roughness, k_o^+, is also given.

surface was located with the two-component LDV probe before measurements were recorded for each baseline flow condition. The experiments were conducted at three flow speeds corresponding to 6 $\mathrm{m\,s^{-1}}$, 12 $\mathrm{m\,s^{-1}}$ and 18 $\mathrm{m\,s^{-1}}$ in the LCC's test section with no model present. Although these nominal flow speeds are used to identify flow conditions throughout this paper, the effect of model blockage, and boundary-layer growth on the model and on the tunnel walls, caused the actual flow speed above the test surface to increase by as much as 10 % (see the second column of table 1).

Compressed air was injected through one of two gas injectors having spans of 2.65 m located at $x = 1.32$ m, the upstream injector (UI), and at $x = 9.79$ m, the downstream injector (DI). The compressed air, filtered to remove particles as small as 1 μm, was supplied to each injector through a 40-port manifold with a port spacing of

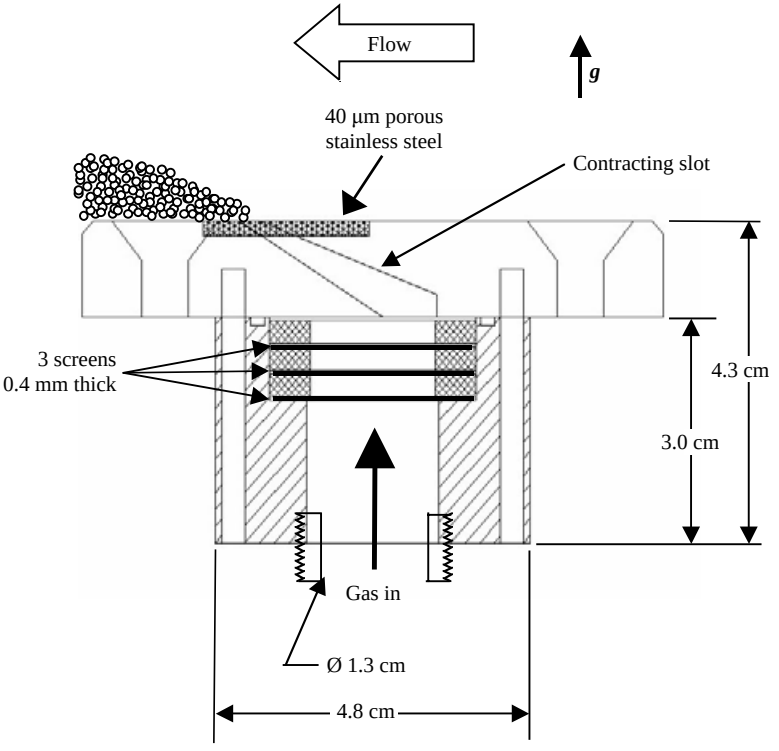

FIGURE 3. Cross-sectional schematic of the gas injectors. The injector measures 2.65 m in the spanwise direction. The gas inlet at the bottom of the injector consists of forty 1.3 cm ports spaced evenly across the span of the injector. Three brass perforated plates with 0.5 mm diameter holes serve to distribute the gas evenly across the injector. The contracting slot has a 10° taper and a 25° mean angle leading to the 40 μm pore-size sintered stainless steel strip.

approximately 6.5 cm. Within the injector, the compressed air passed through three finely-perforated plates (0.5 mm diameter holes on 1 mm centres for 33 % open area, 3.2 mm between plates), a 10° contracting slot with a mean 25° angle, and a sintered stainless steel slab having 40 μm pores (see figure 3). The compressed and filtered air was metered upstream of the injectors using five independent regulating flow meters (0.09 $m^3 s^{-1}$ capacity, Sierra Instruments model 840N3-0-0V1-D-V1-S1-MP). The experiments involved four volumetric airflow rates: $Q_a = 0.05$, 0.09, 0.19 and 0.38 $m^3 s^{-1}$. At the lowest LCC flow speed and the highest air injection rate, the volume flux of water in the test section was approximately 140 times larger than the air volume flux. Alternatively, Q_a/Ubt never exceeded 0.12, where t is the model thickness.

2.2. *Instrumentation*

The primary diagnostic systems employed for these experiments were LDV systems for setting water-flow velocity and measuring profiles without bubbles, static pressure taps, metering air-flow controllers, floating-plate strain-gauge-based skin-friction force balances, and plate-internal and tunnel-external bubble-imaging systems. During the experiments, the water temperature ranged from 17.5°C to 23.3°C. At the three lower air-injection rates, the LCC test-section pressure was typically maintained at approximately 138 kPa (absolute). At the highest gas injection rate (0.38 $m^3 s^{-1}$), a steady rise in test-section pressure occurred to a maximum of 240 kPa as a result of

the gas injection. Ignoring surface-tension effects, such pressure changes cause bubble volume to decrease by ∼40 %, and bubble diameters to decrease by ∼17 %. However, such changes were not observed with the bubble imaging system, indicating that the regulated gas injection pressure gradually rose with increasing tunnel pressure to maintain a nearly steady state over the 1–2 min duration of an individual experiment. Air was purged from the LCC interior following each experiment and prior to further data acquisition.

Static pressure was measured at multiple downstream locations on the wall of the test section above and below the model using a Paroscientific Digiquartz (model 740) pressure transducer that was calibrated with a Druck DP601 standard. The taps had a diameter of 1.6 mm and were located ± 48.3 cm from the vertical centre of the tunnel at x/L locations of 0.00, 0.06, 0.15, 0.21, 0.37, 0.46, 0.62, 0.68, 0.83, 0.93 and 0.98. These measurements were corrected for zero-bias error via a no-flow measurement performed prior to data acquisition and were used to calculate the streamwise pressure gradient along the plate, the free-stream flow velocity outside the plate's boundary layer, and the free-stream acceleration. The uncertainties of these quantities are 1.3 %, 0.5 % and 1.0 %, respectively.

The spatially averaged wall shear stress, $\tau_w = D_f/A$, was determined from six floating-plate strain-gauge force balances that measured the skin-friction drag force, D_f, on a circular flush-mounted surface of area A having a 15.24 cm diameter. These sensors were custom-designed and fabricated at the Applied Research Laboratory at the Pennsylvania State University, and were all located at the same spanwise location (approximately 1/3 span) at $x = 1.96$ m, 3.41 m, 5.94 m, 7.43 m, 9.23 m and 10.68 m (see figure 1). The maximum gap between the sensing surface and the force-balance cup was approximately 75 μm at all points around the circumference, and care was taken to ensure that the sensitive area was levelled and flush with the force balance's housing to within 25 μm. During the levelling process for each sensor, the gap around the circumference of the sensitive area was screened with a metal feeler gauge for uniformity and a minimum clearance of 50 μm. At the highest Reynolds numbers, $l_{v,o}$ is ∼1.7 to 1.8 μm, making the minimum housing-sensitive area gap $\sim 30\, l_{v,o}$. Strain gauge amplifiers (Vishay 2310) were employed for excitation, nulling and amplification of the skin friction signals. Data were collected at a rate of 100 Hz for variable lengths of time ranging from 10 s to several minutes. Measurements reported here represent 10 s averages. The force balances were individually calibrated at least once per test day using a series of masses ranging from 0.25 kg (2.45 N) to 1.25 kg (12.3 N). The standard deviation of the calibration points from a linear fit corresponded to approximately 0.01 N.

For these skin-friction force balances, the significant sources of uncertainty include static pressure sensitivity, drift and calibration errors. Controlled no-flow tests involving only changes in tunnel pressure were used to compensate for pressure changes during experiments to ± 0.07 N. In addition, no-flow measurements at a standard pressure were made several times per day to compensate for drift to ± 0.06 N. The combined random error varied between force balances, but was typically ± 5 % to ± 10 % of any force measurement. This does not include a systematic multiplicative bias error of approximately -7 % arising from either the inadequacy of the static calibration procedure or the geometrical configuration the shear stress sensors. Allen (1977) discusses a variety of possible measurement errors for the type of instrumentation used in this study. Fortunately, the multiplicative bias error is removed once the skin friction ratio, C_F/C_{Fo}, is computed. However, the overall

uncertainty of any C_F/C_{Fo} value is $\pm 10\,\%$ to $\pm 20\,\%$, double the random error of either C_F or C_{Fo} alone.

A Sony XC-55BB progressive-scan black and white miniature digital camera system and a VCL-12YM C-mount lens were used to view the bubbles closest to the surface of the plate through a small window on the surface of the test plate. An external trigger was employed with the camera system, allowing for a shutter-speed as small as 10 μs. The camera's resolution was 659×494 pixels with a pixel dimension of 7.4×7.4 μm. The camera's field of view was 11.0 mm × 8.3 mm. A triangular prism with a ruled surface was used to determine the depth of focus. An in-water focus depth-of-field of 2.1 mm was measured. The camera looked downward from the model, and was mounted on a remote-controlled micro-traverse (Optosigma model SGSP60-5ZF) capable of 1 μm incremental motion over a range of 5 mm. This traverse allowed the camera's focal plane to be placed at different distances from the surface. The camera was adjusted prior to an experiment by setting the furthest limit of its focal field at the wetted surface of the window. Once a bubble injection experiment was begun, if no in-focus bubbles were observed, the camera's focal plane was traversed into the flow (i.e. downward away from the test surface) until the bubbles first came into focus. Thus, images of the bubbles closest to the test surface were recorded. Bubble imaging stations were located at $x = 1.96$ m and 10.68 m with a 4 W argon-ion laser providing illumination via an optical fibre. A digital image acquisition system (BitFlow, model RAV-HCI-110-VNS) was used to acquire the images at 3 f.p.s., and Video Savant (V3.0, IO Industries) digital video recording software was used to process and evaluate the images. Bubble radii were measured graphically for each acceptable (i.e. in-focus) bubble. A test target was used to determine the image's pixel resolution: 18 μm/pixel. Bubble distances from the surface of the model were deduced from the camera's vertical position, and its measured focal characteristics. The measured bubble dimensions were accurate to ± 1 pixel or ± 18 μm. For a bubble diameter of 300 μm, this is an uncertainty of $\pm 6\,\%$. At least 100 bubbles in each of 20 images were examined for each flow condition. In addition, estimates of the bubble translation speed were obtained by increasing the exposure time to 100 or 200 μs to create bubble streak images.

Unfortunately, it was not possible to deduce void fraction, γ, from the two-dimensional bubble images. Rather, the bubble area ratio A_{bubble}/A_{total}, which tends to over-predict γ, was extracted from the images as a surrogate. The area ratio was determined by manually cropping the images to remove those portions that were not of sufficiently high quality for processing, selecting in-focus bubbles, painting them white, changing the rest of the image to black, and then calculating A_{bubble}/A_{total} as the fraction of white pixels in the cropped field (see figure 4).

An external assessment of the size and growth of the bubbly portion of the boundary layer was made with four Pulnix cameras (model TMC-7DSP) and a Panasonic video tape recorder (model AG-1960). The resolution of each camera is 768×494 pixels, or 460 horizontal TV lines. The field of view was approximately 0.6 m wide by 0.4 m high. The cameras were mounted to tripods outside the water tunnel and acquired real-time 30 f.p.s. video of the upstream gas injector and the bubbly layer at $x = 1.96$ m, 5.94 m and 10.68 m. Scales attached to the LCC windows were used to determine visually the thickness of the bubbly layer. Here, uncertainty was associated with identifying the edge of the bubble cloud. At $x = 1.96$ m, the edge was fairly well defined, leading to a thickness uncertainty of ± 0.6 cm. Further downstream, the bubble-layer edge was less defined, and the layer thickness uncertainty was ± 2 cm.

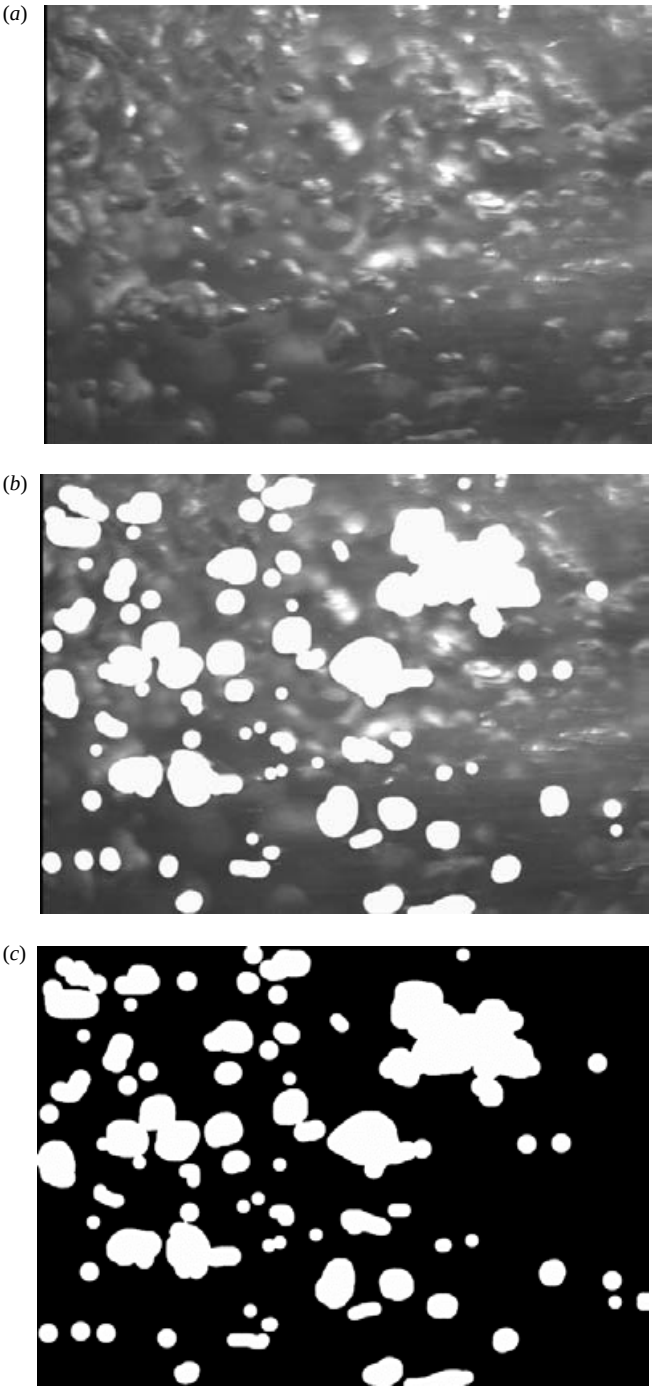

FIGURE 4. Illustration of the image processing to determine the area ratio from a bubble images. (*a*) Bubble images from $x = 10.68$ m with the camera's focus field placed 1.0 mm from the surface of the model at a nominal free-stream velocity of $12\,\mathrm{m\,s^{-1}}$ with upstream injection at $0.19\,\mathrm{m^3 s^{-1}}$. (*b*) The image shown in (*a*) after highlighting the focused bubbles. (*c*) The image shown in (*b*) after binarization; this image represents a 20 % area ratio. The undistorted image size is 1.1 cm by 0.83 cm. The flow is from right to left.

3. Results

3.1. *Baseline boundary layer characteristics*

The characteristics of the single-phase boundary layer were measured in preliminary tests without bubble injection. These results are summarized in table 1 where boundary-layer flow quantities are given at the six locations of the force balances. Here, Re_x is calculated from $Re_x = \int_0^x U\,\mathrm{d}x/\nu$ to account for the mild increase in U, with $\nu = 9.96 \times 10^{-7}\,\mathrm{m^2\,s^{-1}}$ based on the average measured water temperature of 20.4 °C. The third column in table 1 provides Patel's acceleration parameter,

$$K' = \frac{\nu}{U^2}\frac{\mathrm{d}U}{\mathrm{d}x}. \tag{3.1}$$

Patel (1965) determined that the influence of the pressure gradient on the mean boundary-layer velocity profile is small for $K' < 1.63 \times 10^{-6}$. The values of K' in this study are typically more than three orders of magnitude smaller than this limit. Table 1 also gives a calculated difference, $\delta_o - \delta_o^*$, between the 99 % thickness (δ_o) and displacement thickness (δ_o^*) for an unmodified zero-pressure-gradient boundary layer (Schlichting 1979) based on

$$\delta_o - \delta_o^* = 0.324x\,(Re_x)^{-1/5}. \tag{3.2}$$

When multiplied by U, this difference represents an estimate of the volumetric flow rate of liquid in the boundary-layer per unit span. Table 1 also provides boundary-layer momentum thickness, θ_o. At $x = 10.68\,\mathrm{m}$, θ_o was determined from LDV measurements. The values of θ_o for other measurement locations were calculated from

$$\theta_o = 0.0364x\,(Re_x)^{-1/5}. \tag{3.3}$$

The baseline wall unit, $l_{v,o} = \nu/u_o^*$, is tabulated for each condition. Lastly, the dimensionless surface roughness,

$$k_o^+ = ku_o^*/\nu, \tag{3.4}$$

is given. Here, k_o^+ is comfortably less than one, so the plate was hydraulically smooth (White 1991).

3.2. *Surface shear stress measurements*

The spatially averaged surface shear stress measurements, without air injection, are presented in figure 5 as C_{Fo} *vs.* Re_x, along with the skin-friction line of Schultz-Grunow (1941). A least-squares fit of the measured data yields a power-law relationship between C_{Fo} and Re_x,

$$C_{Fo} = (0.025 \pm 0.002)Re_x^{-(0.149\pm0.017)}. \tag{3.5}$$

Given that most prior skin friction correlations lie near the Schultz-Grunow line (Nagib *et al.* 2004), the current results appear to be systematically biased approximately 7 % low. The sources of this bias error are believed to be friction in the pulleys used during sensor calibration, and possible leakage flow through and around the sensors.

Measured skin friction ratio, C_F/C_{Fo}, *vs.* downstream distance x is shown in figure 6 for all three test speeds and all four air injection rates when air was injected at $x = 1.32\,\mathrm{m}$ (UI). Here, measured values of C_F/C_{Fo} that fell below $C_F/C_{Fo} = 0$ because of experimental errors have been plotted at $C_F/C_{Fo} = 0$, and the shear stress sensor at $x = 5.94$ was not functioning reliably during these tests so its output has not been plotted. The figure 6 results span a range of air flow morphologies. Data

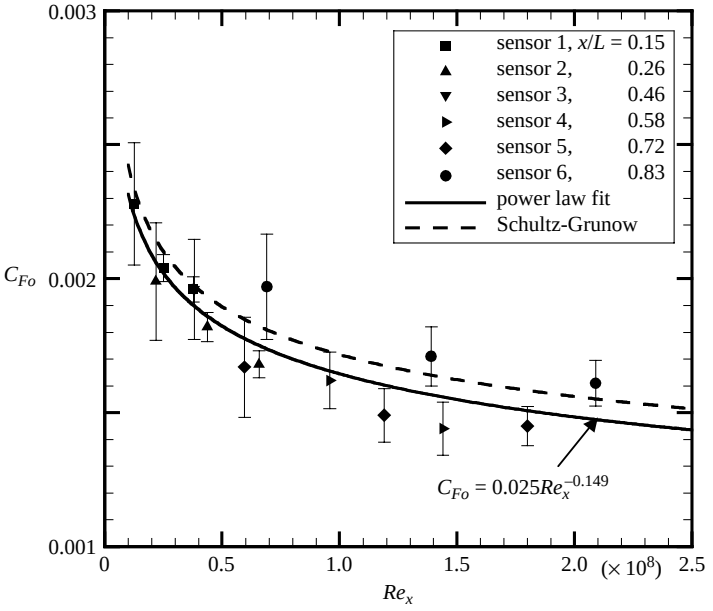

FIGURE 5. Skin friction coefficient, C_{Fo}, in the absence of bubbles as a function of Reynolds number (based on downstream distance). A power-law least-squares fit to the shear stress data is shown as a solid line. The classic friction line of Schultz-Grunow (1941) is shown as a dashed line for comparison.

points connected by solid lines correspond to bubbly flows. Data points connected by dashed lines correspond to flows where either an intermittent or a continuous air-layer formed on the surface of the test plate. In addition, the $12\,\mathrm{m\,s^{-1}}$ and $0.38\,\mathrm{m^3\,s^{-1}}$ flow condition, denoted by a dotted line in figure 6, was a composite patchwork of bubbles and air film. The thin vertical line at $x = 1.32$ denotes the air injector location. The primary finding shown on figure 6 is the loss of drag reduction in the bubbly flows a few metres downstream of the air injector compared to the air film cases where drag reduction persisted with increasing x.

When the air flow rate is normalized, the figure 6 results can be compared to prior BDR experiments on smooth flat surfaces. Figure 7 shows C_F/C_{Fo} *vs.* $Q_a/(Q_a + Q_w)$. Although the data are scattered, some agreement is evident for datasets obtained in the same facility under similar conditions (i.e. varying injection flow rates, but common injection and measurement locations). Overall, the collapse is not particularly good across the breadth of the flat-plate BDR data, except for the two trends that C_F/C_{Fo} approaches unity for small abscissa values (0.1) and that C_F/C_{Fo} generally decreases with increasing gas injection. Some of the scatter arises from the orientation of the measurement surface with respect to gravity becoming significant at low speeds (e.g. for U $6\,\mathrm{m\,s^{-1}}$) because of bubble buoyancy, and this is not accounted for by the dimensionless scaling used in figure 7.

Figure 8 exhibits two additional ways of normalizing the air flow rate in BDR experiments. Figure 8(*a*) shows the present data along with the results of Deutsch *et al.* (2003) using $Q_a/(Q_a + U\theta_o b)$ as the abscissa. Here, the momentum thickness without air injection, θ_o, replaces $\delta_o - \delta_o^*$ from figure 7, and there is an improvement in the agreement between the upstream injection results at $12\,\mathrm{m\,s^{-1}}$ and $18\,\mathrm{m\,s^{-1}}$, and

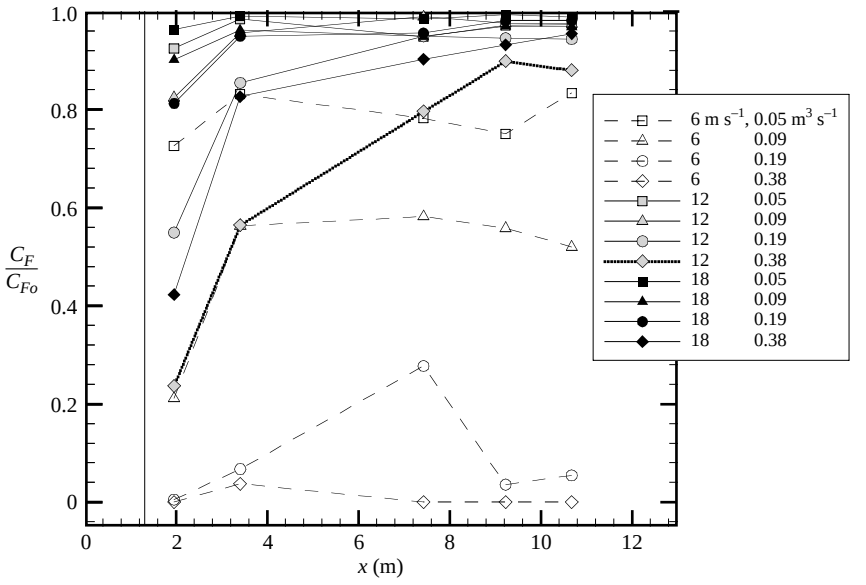

FIGURE 6. Skin friction ratio C_F/C_{Fo} as a function of downstream distance x (in metres) for upstream injection. Error bars are not shown for clarity but would be $\pm 10\,\%$ to $\pm 20\,\%$ of each measurement. Data points connected by solid lines represent flow conditions having distinct bubbles. Data points connected by dashed lines represent flow conditions leading to a continuous or intermittent gas film on the surface of the test model with only occasional patches of bubbles. The $12\,\mathrm{m\,s^{-1}}$ and $0.38\,\mathrm{m^3\,s^{-1}}$ test condition shown with a dotted line produced both bubbles and gas film in nearly equal amounts. Measured values of C_F/C_{Fo} that fell below $C_F/C_{Fo} = 0$ because of experimental errors have been plotted at $C_F/C_{Fo} = 0$. The thin vertical line at the left-hand edge of the figure marks the location of the upstream injector.

the results of Deutsch *et al.* (2003). The upstream injection results for $6\,\mathrm{m\,s^{-1}}$ and the downstream injection results for all flow speeds do not follow the overall trend.

The current $6\,\mathrm{m\,s^{-1}}$ results are not expected to agree with the other measurements because of intermittent or continuous air-film formation on the model surface at this flow speed. When these data are excluded, the downstream injection measurements at the higher flow speeds collapse better by including a correction for the boundary-layer momentum thickness at the location of the injector in the normalization of the air flow rate, $Q_a/(Q_a + U(\theta_o - \theta_{o,inj})b)$. This improved data collapse is shown in figure 8(*b*) using the present $12\,\mathrm{m\,s^{-1}}$ and $18\,\mathrm{m\,s^{-1}}$ cases with data from Deutsch *et al.* (2003). Although reasonably successful, this normalization is *ad hoc* and the visual improvement in the data collapse between figure 8(*a*) and 8(*b*) may have more to do with the algebra than bubbly-boundary-layer physics. For example, when the boundary-layer length scale – generically labelled δ in (3.6) below – approaches zero, the limit of the air flow rate scaling becomes unity, i.e.

$$\lim_{\delta \to 0} \frac{Q_a}{Q_a + U\delta b} = 1 \quad \text{when } Q_a \neq 0, \tag{3.6}$$

independent of the value of Q_a. Thus, when $U\delta b$ is much smaller than $Q_{a,i}$, the value of Q_a necessary to initiate non-zero BDR, all measured BDR data would lie on a horizontal line near $C_F/C_{Fo} = 1$ when $Q_a < Q_{a,i}$, while all other BDR data would lie

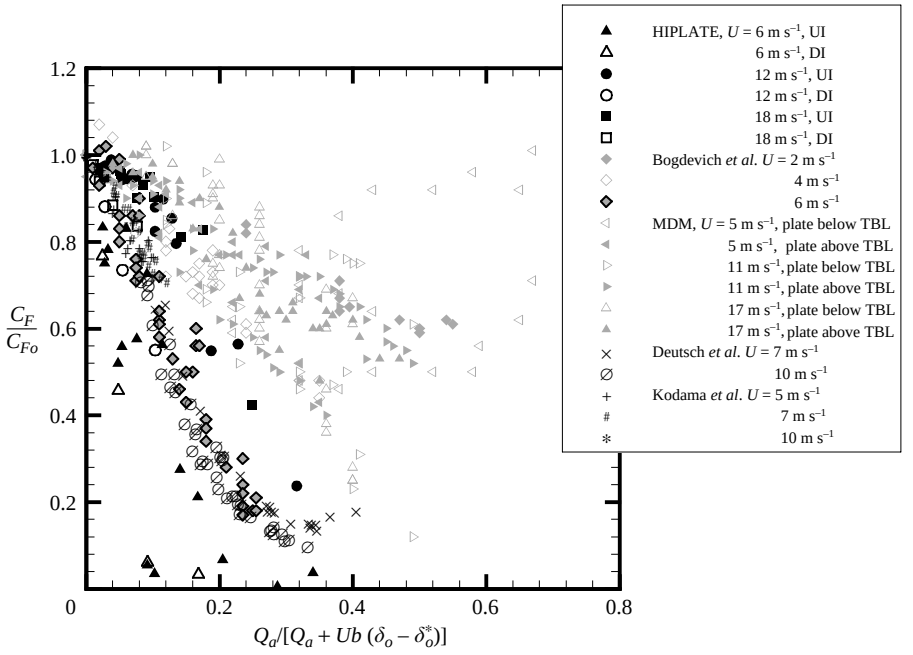

FIGURE 7. Skin friction ratio as a function of the volumetric fraction of gas flow rate (1.2) for the present work, compared to the results of previous researchers. UI = upstream air injection at $x = 1.32$ m; DI = downstream air injection at $x = 9.79$ m. The data from Bogdevich *et al.* represent those acquired by Soviet researchers (1974–1976) in plate-up and plate-down experiments. MDM, data reported by Madavan, Deutsch & Merkle (1984, 1985*a*).

on a nearly vertical line at $Q_a/(Q_a + U\delta b) = 1$. Unfortunately, neither figure 7 nor figure 8 provide an adequate collapse of the BDR data and therefore are of limited use for predicting the persistence of BDR.

3.3. *Bubbly flow characteristics and mean bubble sizes*

Images of the air-injected flow looking from the plate at $x = 1.96$ m and 10.68 m at all three flow speeds were used to determine the near-surface bubble characteristics: size, distance from the surface, relative abundance near the wall, and apparent convection speed. Figure 9 presents six representative images arranged from greatest to least skin-friction drag reduction. Each image in figure 9 shows an area approximately 9 mm wide (streamwise direction) by 8 mm high (spanwise direction) with the flow direction from right to left. Figure 9(*a*) ($x = 1.96$ m, upstream air injection at $0.38\,\mathrm{m^3\,s^{-1}}$, $6\,\mathrm{m\,s^{-1}}$) shows an air-film condition where $C_F/C_{Fo} \approx 0$, ~100 % BDR. The focal plane of the camera was 1.0 mm from the surface of the model and capillary waves on the air–water interface are apparent in the upper right-hand corner of the image. Figure 9(*b*) ($x = 1.96$ m, upstream air injection at $0.38\,\mathrm{m^3\,s^{-1}}$, $12\,\mathrm{m\,s^{-1}}$) shows a bubbly flow leading to $C_F/C_{Fo} = 0.24$ (76 % BDR). The focal plane of the camera was 0.5 mm from the surface of the model. Here, bubble radii varied from 50 to 750 μm with an average of ~150 μm, and an air film was intermittently present at this condition. Figure 9(*c*) ($x = 1.96$ m, upstream air injection at $0.38\,\mathrm{m^3\,s^{-1}}$, $18\,\mathrm{m\,s^{-1}}$) shows a higher-speed bubbly flow leading to $C_F/C_{Fo} = 0.42$ (58 % BDR). The focal plane of the camera was again positioned 0.5 mm from the surface of the model, but

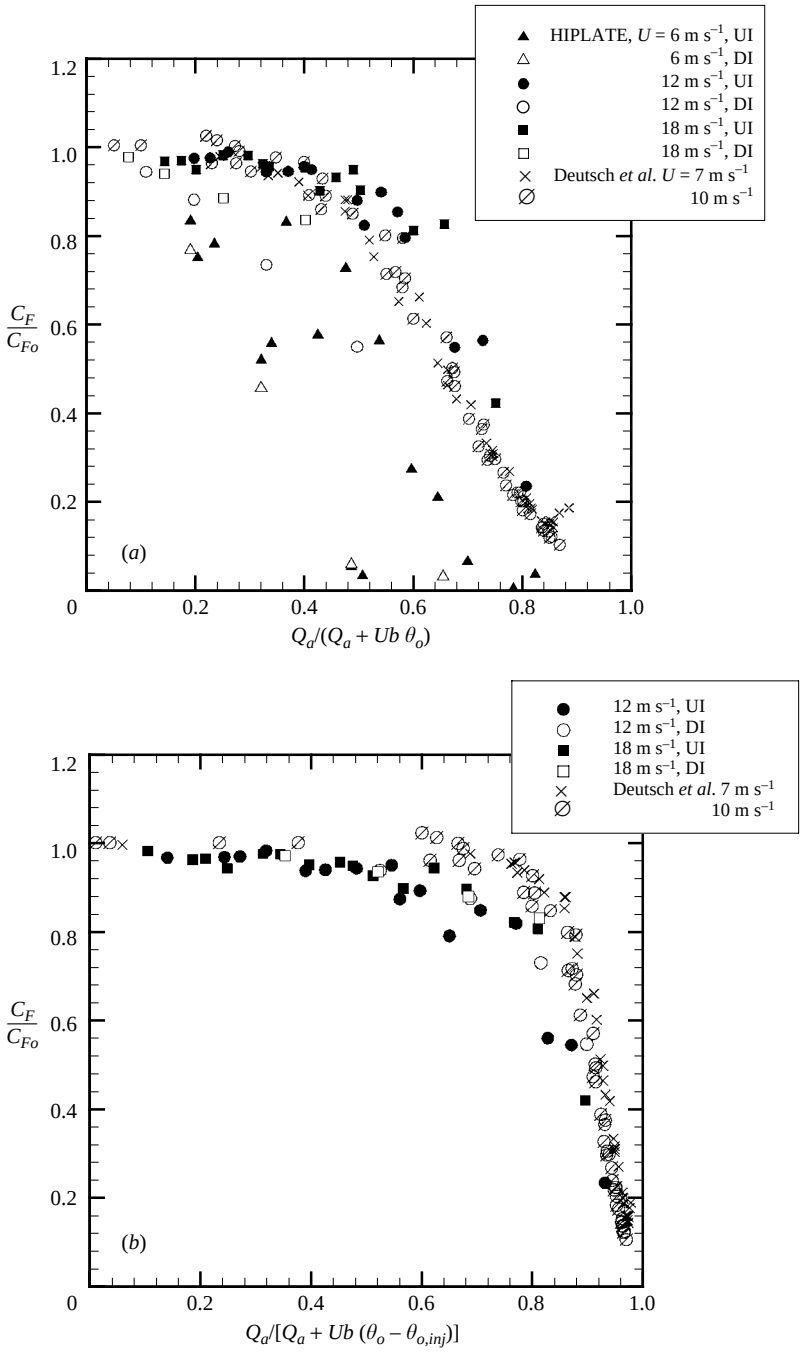

FIGURE 8. (*a*) Skin friction ratio as a function of flux-based void fraction using the momentum thickness of the unmodified boundary layer, θ_o. (*b*) Skin friction ratio as a function of the rescaled gas flow rate, where $\theta_{o,inj}$ is the estimated momentum thickness of the unmodified boundary layer at the streamwise location of the gas injector. The smooth-wall data presented by Deutsch *et al.* (2003) are also plotted.

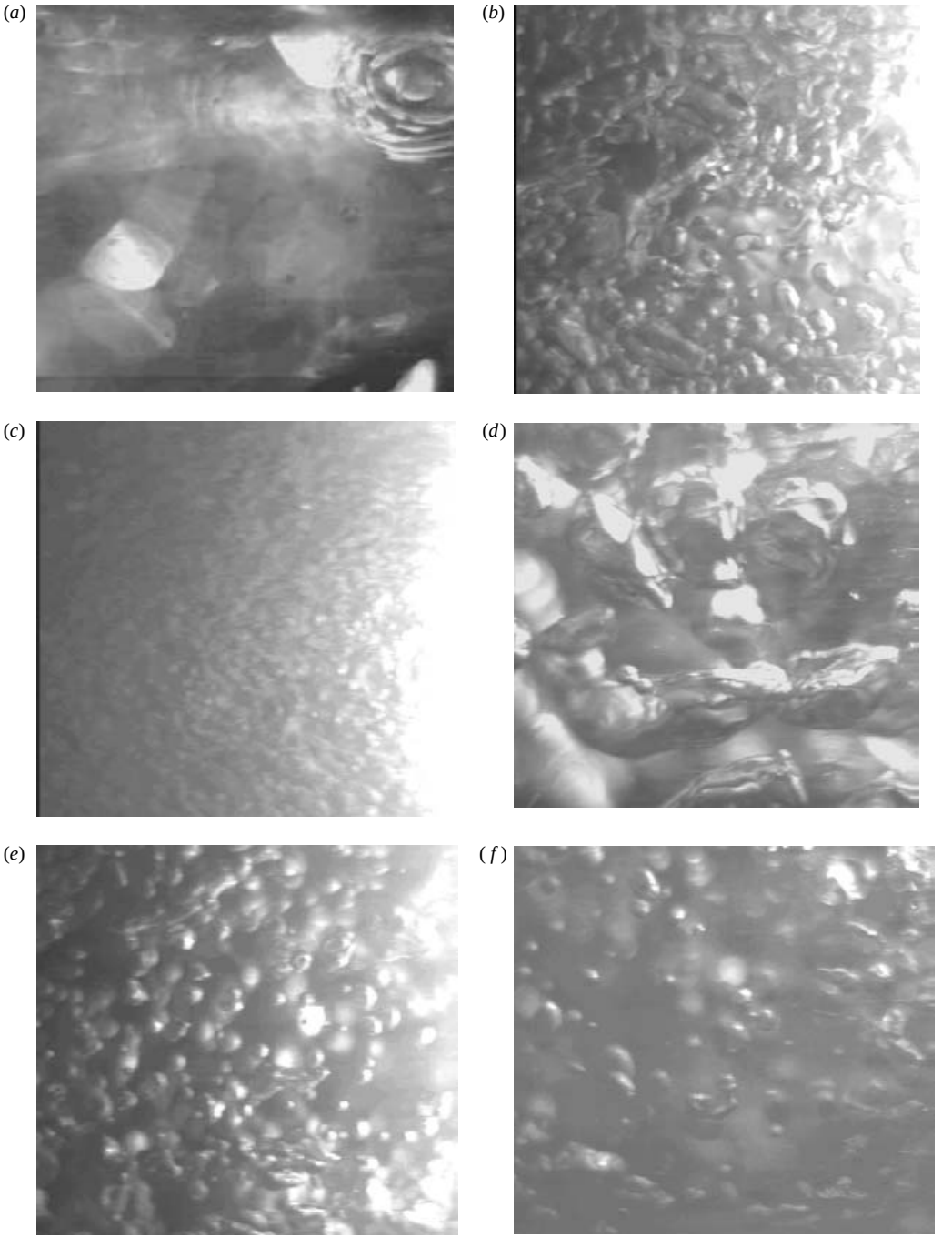

FIGURE 9. Images recorded by the bubble camera for upstream gas injection. The nominal frees-tream velocity, gas flow rate, measurement location, BDR percentage, and camera focal plane distance from the test surface for each image are: (*a*) 6 m s^{-1}, 0.38 m^{3}s^{-1}, 1.96 m, ∼100 %, 1.0 mm; (*b*) 12 m s^{-1}, 0.38 m^{3}s^{-1}, 1.96 m, 76 %, 0.5 mm; (*c*) 18 m s^{-1}, 0.38 m^{3}s^{-1}, 1.96 m, 58 %, 0.5 mm; (*d*) 6 m s^{-1}, 0.09 m^{3}s^{-1}, 10.68 m, 48 %, 1.0 mm; (*e*) 12 m s^{-1}, 0.09 m^{3}s^{-1}, 1.96 m, 18 %, 0.5 mm; (*f*) 12 m s^{-1}, 0.38 m^{3}s^{-1}, 10.68 m, 12 %, 0.5 mm. Each image represents approximately 9 mm (horizontal) by 8 mm (vertical). Flow is from right to left.

U (m s^{-1})	Q_a (m^3 s^{-1})	u^* (m s^{-1})	y_b (mm)	D_{max}(μm)	D(μm)
12.76	0.05	0.39	0.5–1.0	220–290	350 ± 150
	0.09	0.37	0.5–1.0	230–310	320 ± 130
	0.19	0.30	0.5–1.0	300–390	410 ± 140
19.21	0.05	0.58	1.0–1.5	180–210	230 ± 100
	0.09	0.57	1.0–1.5	180–210	200 ± 70
	0.19	0.54	0.5–1.0	150–200	220 ± 80
	0.38	0.38	0.5–1.0	220–300	200 ± 50

TABLE 2. Comparison of the maximum diameter range, D_{max} (3.7), to the measured diameters of the imaged bubbles, D, at varying flow speeds, gas injection rates, and bubble heights in the boundary layer, y_b. All the tabulated results are at $x = 1.96$ m with upstream injection at $x = 1.32$ m. The value of u^* is based on the measured skin friction during gas injection. The column for the bubble diameter, D, gives the average bubble diameter and plus or minus one standard deviation.

the presence of more out-of-focus bubbles compared to figure 9(*b*) suggests that the bubbles are farther from the surface. Here, bubble radii varied from 15 to 250 μm with an average of ∼100 μm. Figure 9(*d*) ($x = 10.68$ m, upstream air injection at 0.09 m^3 s^{-1}, 6 m s^{-1}) shows a transition condition between distinct bubbles and an intermittent air-film where $C_F/C_{Fo} = 0.52$ (48 % BDR). The focal plane of the camera was 1.0 mm from the surface of the model. Figure 9(*e*) ($x = 1.96$ m, upstream air injection at 0.09 m^3 s^{-1}, 12 m s^{-1}) shows a bubbly flow that merely achieved $C_F/C_{Fo} = 0.82$ (18 % BDR). The focal plane of the camera was positioned 0.5 mm from the surface of the model. Here, the bubbles are similar in appearance and reside at the same distance from the test surface as those shown in figure 9(*b*) for the same geometry and water flow conditions at a higher air flow rate. However, in figure 9(*e*) the bubbles are slightly larger (average radius of 175 μm) and are far fewer in number than those in figure 9(*b*). Figure 9(*f*) ($x = 10.68$ m, upstream air injection at 0.38 m^3 s^{-1}, 12 m s^{-1}) shows a bubbly flow with $C_F/C_{Fo} = 0.88$ (12 % BDR). The focal plane of the camera was 0.5 mm from the surface of the model. Here, the bubbles are larger (average radius of 250 μm) and sparser than the identical injection and flow conditions upstream on the plate at $x = 1.96$ m, figure 9(*b*). In addition, the majority of the bubbles are out-of-focus, indicating that they are farther from the test surface. Overall, these bubble images and the BDR numbers indicate that the presence of many bubbles near the surface produces more BDR than fewer bubbles farther from the surface, a confirmation of the main conclusion of prior studies.

As hypothesized by Hinze (1955), the maximum stable bubble size, D_{max}, in a turbulent flow can be related to the interfacial tension σ, the fluid density ρ, and the turbulent kinetic energy dissipation rate ε, by

$$D_{max} \approx (\sigma/2\rho)^{3/5}\varepsilon^{-2/5} \approx (\sigma/2\rho)^{3/5}(\kappa y/(u^*)^3)^{2/5}. \tag{3.7}$$

The second approximate equality should hold in the log region of a turbulent boundary layer where $\varepsilon = (u*)^3/\kappa$y with $\kappa =$ the von Kármán constant, and $y =$ the wall normal coordinate (Pope 2000). Thus, the critical bubble diameter in clean water (i.e. $\sigma = 0.073$ N m^{-1}) should also depend on the vertical location of the bubble and the friction velocity.

The observed bubble distances from the surface (discussed below) can be used to estimate the critical bubble diameter using (3.7). Table 2 presents the estimated maximum diameter before bubble breakup compared with the measured mean and

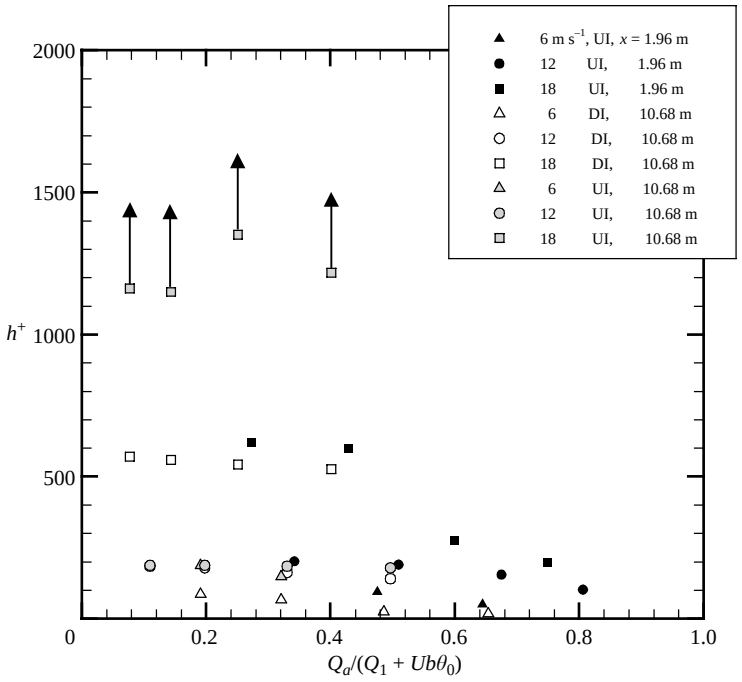

FIGURE 10. Non-dimensional vertical distance, h^+, from the test surface to the bubbles nearest the test surface (bubbly flows) or to the air–water interface (gas-film flows) as a function of flux-based void fraction; UI = upstream air injection at $x = 1.32$ m; DI = downstream air injection at $x = 9.79$ m. These heights represent the distance to the approximate centre of the camera focal volume when it was vertically traversed to observe in-focus bubbles or the air–water interface. The variability associated with these h^+ data are $\pm 250\,\mu$m which corresponds to a range of approximately ± 50 to ± 150 wall units for the set of nominal free-stream speeds of 6, 12 and 18 m s^{-1}. Data points with arrows indicate that the bubbles were too far from the surface of the model to bring them fully into focus via adjustments to the bubble imaging system.

standard deviation of bubble diameter (figure 11 presents bubble size histograms). As found by Pal *et al.* (1988), the estimated and measured diameters correspond fairly well, suggesting that bubble breakup would only have occurred upstream of $x =$ 1.96 m, if at all. Thus, it is unlikely that bubble breakup is the primary mechanism for the continued presence of BDR at $x = 1.96$ m where the bubbles were observed. This is supported by the observation that the bubbles are not highly distorted by the turbulent flow, suggesting that they have reached a nearly equilibrated size.

3.4. *Bubble locations relative to the surface*

Figure 10 shows the dimensionless height, $h^+ = hu^*/\nu$ using the bubbly-flow $u*$, of the bubbles nearest the surface of the model *vs.* $Q_a/(Q_a + U\theta_o b)$. These heights represent the distance from the wall through which the outer edge of the camera's focal field was moved to observe in-focus bubbles. The uncertainty of this measurement was $\pm 250\,\mu$m, which corresponds to a range of ± 50 to ± 150 wall units for the nominal free-stream speeds of 6, 12 and 18 m s^{-1}. The inner-variable normalization of the height was chosen to see whether near-wall bubbles reach an equilibrium height within the boundary layer. The upward-pointing arrows in figure 10 indicate that

the bubbles were beyond the combined limit of the camera's maximum focal plane height and depth-of-field. This situation occurred at the downstream camera location, $x = 10.68$ m, and at the highest flow speeds during upstream injection. Figure 10 shows that bubbles tended to stay slightly closer to the surface at higher injection rates for the same flow speeds and injection locations. This is caused, at least in part, by the fact that as the gas injection rate increases, the skin friction decreases, resulting in an increase in l^+. In addition, these results show that inner variable scaling does not collapse bubble height, although the scaled bubble heights do trend similarly for both upstream and downstream injection. Incidentally, the bubble heights shown in figure 10 are consistent with the simple bubble-image velocimetry results which showed the average bubble velocity divided by the free-stream speed was as low as 0.30 when C_F/C_{Fo} was appreciably below unity, but rose to between 0.50 and 0.65 when C_F/C_{Fo} was near unity.

The most important finding shown in figure 10 is obtained in conjunction with figure 6. When combined, the two figures demonstrate that BDR is lost when a nearly bubble-free liquid layer forms on the surface of the plate, and this appears to be the primary phenomenon limiting BDR persistence. As discussed further in § 4, shear-induced bubble migration is a possible mechanism for the development of this nearly bubble-free liquid layer.

3.5. *Bubble size distributions and coalescence*

Bubble sizes and the extent of bubble coalescence varied with downstream distance and flow speed. For the $6\,\mathrm{m\,s^{-1}}$ conditions, the injected bubbles coalesced into an intermittent or continuous air film. At higher speeds, discrete bubbles were observed all along the plate. However, the number of bubbles and their size distribution changed as the bubbles moved downstream. Figure 11(*a*) shows a typical distribution of the diameters of 100 randomly selected bubbles imaged at $x = 1.96$ m and 10.68 m for $12\,\mathrm{m\,s^{-1}}$ when $Q_a = 0.05$, 0.09 and 0.19 $\mathrm{m^3\,s^{-1}}$. Figure 11(*b*) shows the same information for $18\,\mathrm{m\,s^{-1}}$ when $Q_a = 0.05$, 0.09, 0.19 and $0.38\,\mathrm{m^3\,s^{-1}}$. For bubble images that were not well focused, the diameter estimates and hence histograms are more qualitative. The mean diameter and the average number of bubbles per $\mathrm{cm^2}$ are also tabulated in the figure. For both flow speeds, the mean bubble diameter increases by an average of about 30 %, while the number density decreases by 50 to 80 % between $x = 1.96$ m and 10.68 m. The increase in the mean diameter suggests that the bubbles are coalescing. Consider the coalescence of two 200 μm diameter bubbles. The resulting larger bubble will have a diameter of $200(2)^{1/3} = 252$ μm, an increase of 26 %. Bubble diameter increases of this size were observed between $x = 1.96$ m and 10.68 m. With such two-to-one coalescence, the number density of the bubbles should decrease by a factor of two. However, the measured number density is reduced by a factor of 2 to 4. The additional number density reduction is probably a result of dilution as the boundary layer entrains liquid. The increase in the mean diameter, in addition to the decrease in the overall number of bubbles, suggests that there is bubble coalescence, even though there is probably some production of smaller bubbles as well.

The effect of gas diffusion on bubble volumes should be negligible in these tests. The tunnel water was saturated with air at atmospheric pressure during the repeated injection-and-purge test cycle. During injection, the free-stream pressure was consistently higher than atmospheric pressure, suggesting that some of the injected gas could re-dissolve as the bubbles moved over the model. Dissolution will occur if the water is under-saturated and if the Laplace pressure leads to diffusion into the water. We can compare the Laplace pressure, $0.1\,\mathrm{kPa} < 2\sigma/R < 10\,\mathrm{kPa}$ (with $\sigma = 0.073\,\mathrm{N\,m^{-1}}$),

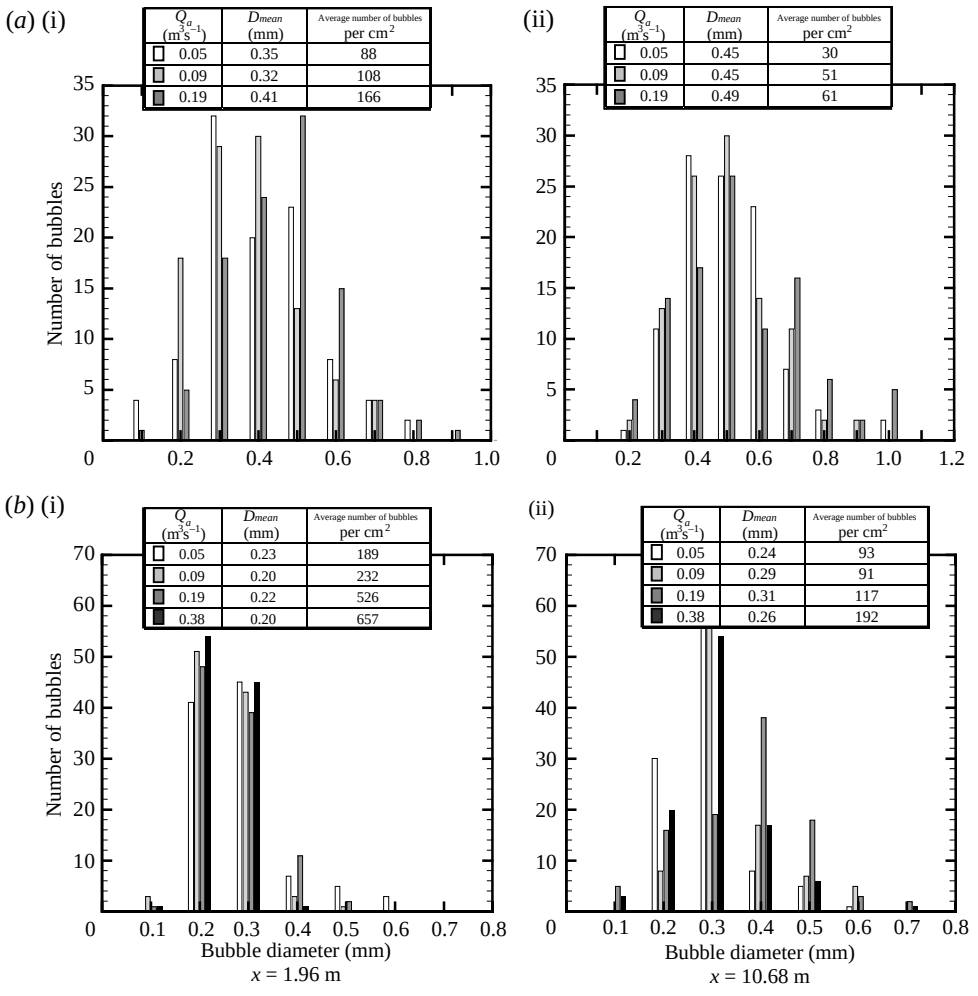

FIGURE 11. Histograms of bubble diameters imaged during upstream injection at (*a*) 12 m s^{-1} for three injection rates and (*b*) 18 m s^{-1} flow conditions for all four injection rates. For each histogram, 100 bubbles were randomly selected and measured; the measured diameter was rounded to the nearest 100 µm. The mean diameter, D_{mean}, and number density (per unit area) are tabulated for each condition. For (*b*)(ii), the bubble images were not well-focused so these diameter estimates and hence histograms are more qualitative. Limitations imposed by the imaging system and image-processing techniques conservatively place the error associated with any single bubble diameter measurement at ±50 % for bubble diameters of 0.1 to 0.3 mm, and ±25 % for larger bubble diameters.

to the free-stream pressure, approximately 150 kPa. Consequently, the contribution of the Laplace pressure to bubble dissolution is negligible for the range of bubble sizes observed. The dissolution rate of the bubbles owing to concentration gradients is also expected to be small. The dissolution time for small bubbles, t_D, is approximately

$$t_D \approx \frac{\rho_b R^2}{2\alpha(c_s - c_\infty)} \frac{1}{Nu}, \tag{3.8}$$

where $(c_s - c_\infty)$ is the difference in gas concentration of the water at the bubble interface and far from the bubble, α is the molecular mass diffusivity, and ρ_b is the

gas density. *Nu* is the Nusselt number and is defined as the ratio of the turbulent and molecular mass diffusivity (Gowing 1992; Yu & Ceccio 1997). Gowing (1992) examined the relationship between the Nusselt number and the turbulent Péclet number, *Pe*, for the dissolution of bubbles in a turbulent flow, where

$$Pe = \left(\frac{\varepsilon}{\nu}\right)^{1/2} \frac{R^2}{\alpha}. \tag{3.9}$$

He showed that

$$Nu \approx 0.12 Pe^{1/2} \tag{3.10}$$

for bubbles with radii between 10 and 80 μm in turbulent pipe flows with Reynolds numbers ranging from 10^4 to 10^5. Using the boundary-layer dissipation rate mentioned above, (3.9) and (3.10), the expected range of Nusselt numbers is O(1) to O(10). Then, $0.01 < t_D(c_s - c_\infty) < 0.1\,\mathrm{m^3\,s\,kg^{-1}}$.

Here, the gas diffusion is driven by the concentration difference $(c_s - c_\infty)$. Given the large quantities of air injected, the water was saturated with air at testing pressure, and $(c_s - c_\infty) \approx 0$ for most tests. However, for the highest flow speeds, the free-stream pressure continued to rise as air was injected into the tunnel, and this resulted in an increase in the saturation concentration, c_s. In the worst case presented here (the $18\,\mathrm{m\,s^{-1}}$ runs with the highest gas fluxes), the pressure increased as high as 240 kPa from 138 kPa over a period of several minutes. The resulting rise in the free-stream saturation level would lead to bubble dissolution over relatively short time scales when $(c_s - c_\infty) \approx 0.1\,\mathrm{m^3\,kg^{-1}}$. However, an initial period of injection occurred before acquiring the data, and this produced a flood of gas bubbles into the tunnel flow that convected to the high-pressure regions of the LCC lower leg. The continued presence of gas bubbles in the free stream of the test section once the flow had recirculated, indicates that the tunnel water remained saturated with gas, even as the pressure rose in the test section. The bubbles convecting throughout the test loop would have time to dissolve into the freestream before the flow returned to the test section. Consequently, it is reasonable to assume that $(c_s - c_\infty) \approx 0$ in the test section as the pressure slowly elevated.

3.6. *Near-wall phase composition measurements and persistence*

The results obtained from the bubble images indicate that the size and location of the bubbles are significant parameters for BDR. The images in figure 9 also qualitatively indicate that there is a relationship between the concentration of bubbles near the wall and the degree of drag reduction. The relationship between the measured skin friction ratio and the observed area ratio, A_b/A_{total} (see § 2.2), is shown in figure 12 for the 12 and $18\,\mathrm{m\,s^{-1}}$ cases. Again, the $6\,\mathrm{m\,s^{-1}}$ results were not included owing to air-film formation. For the two $18\,\mathrm{m\,s^{-1}}$ cases where no focused bubbles were found ($x = 10.68$ m, upstream injection, $Q_a = 0.19$ and $0.38\,\mathrm{m^3\,s^{-1}}$), nearly focused bubbles were used instead. Thus, the area ratios for these two points have additional uncertainty associated with them. Given the uncertainties, figure 12 qualitatively indicates that an increase in area ratio (which is monotonically related to void fraction) produces a decrease in drag. These results agree well with the channel flow trends reported by Guin *et al.* (1996) with the drag reduction correlating closely with the near-wall void fraction. The substantial differences in drag reduction between flow conditions that produce similar area ratios (e.g. $12\,\mathrm{m\,s^{-1}}$ and $18\,\mathrm{m\,s^{-1}}$ with upstream injection at $x = 1.96$ m) is attributable to the position of the bubbles with respect to the surface. Specifically, the results presented in figure 10 indicate that the bubbles at $12\,\mathrm{m\,s^{-1}}$ remained nearer to the surface than those at $18\,\mathrm{m\,s^{-1}}$ under

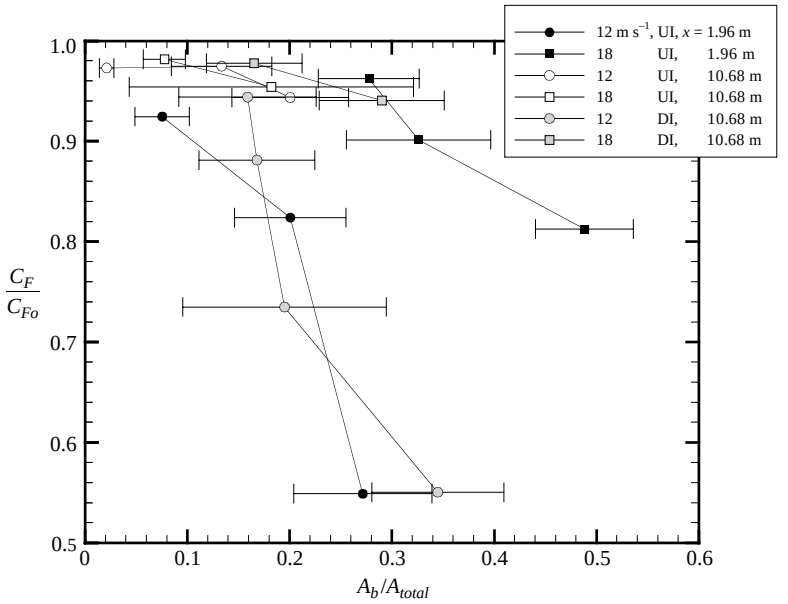

FIGURE 12. The measured skin friction ratio as a function of the imaged area ratios, given by A_b/A_{total}, where A_b is the area of the image covered by focused bubbles and A_{total} is the total area of the image for 12 and 18 m s^{-1}. UI = upstream air injection at $x = 1.32$ m; DI = downstream air injection at $x = 9.79$ m. Vertical error bars of $\pm 10\,\%$ to $\pm 20\,\%$ have not been plotted for clarity. For the two 18 m s^{-1}, UI, x = 10.68 m data points (0.19 and 0.38 m^{3}s^{-1} gas injection rates), the bubbles could not be fully focused so bubble images with some blurring were used to estimate the area ratio. Hence, the area ratio error associated with these two data points is increased. The error bars presented are the standard deviation of the area ratio determined directly from the images analysed.

otherwise identical conditions. However, the results from the 12 m s^{-1} and 18 m s^{-1} cases, although distinct, exhibit similar trends in drag reduction with increasing area ratio for both injection locations. These observations indicate that the relationship between void-fraction and drag-reduction is not critically dependent on the thickness of the boundary layer as set by the location of injection. This suggests that any success in scaling of drag reduction with outer variables like the total boundary-layer thickness may be fortuitous, and that scaling with near-wall variables (such as the near-wall void fraction) may be more appropriate.

Note that the largest area ratio (18 m s^{-1} with upstream injection at $x = 1.96$ m) does not correspond to the case of the greatest drag reduction. Rather, it is the combination of large void fraction with small bubbles in close proximity to the wall that generates drag reduction. Discarding the effects of buoyancy in the 6 m s^{-1} cases, such conditions tend to be mutually exclusive. That is, the bubbles tend to remain closer to the wall at lower speeds, but faster speeds generate smaller bubbles from the same injector. It appears, however, that for the range of bubble sizes generated in this set of experiments, the abundance and proximity of the bubbles to the wall is more important than the bubble size in producing significant BDR.

The area ratio results in figure 12 also argue that BDR is not merely an effect of reduced density. The area ratio is an over-estimate of the local void fraction. Consider mono-disperse spheres in the face-centred-cubic configuration. The volume ratio of the spheres is 0.74, while an image of the spheres taken at a planar boundary

and processed with the algorithm described above would yield an area ratio of 0.79. Inspection of figure 12 shows that an area ratio of ~30 % yields a drag reduction of ~45 %. This suggests that the observed BDR cannot be due solely to a reduction in density, since the skin friction is reduced in higher proportion than the reduction in near-wall density.

4. Bubble stratification and mixing

The migration of the bubbles from the solid surface significantly influences the effectiveness and persistence of bubble drag reduction. This section presents a simple analysis of force ratios that suggests that both buoyancy-induced air films and shear-induced nearly bubble-free liquid layers can form within the parametric ranges explored by the present experiments.

Discrete bubbles in the gas-liquid mixture experience a buoyancy force, and lift and drag forces as turbulent velocity fluctuations produce a relative velocity between the bubble and the surrounding shear flow. The formation of a low-void-fraction layer, e.g. bubble stratification, has been observed when buoyancy acts to move bubbles away from the solid surface as discussed in Pal *et al.* (1988). Conversely, buoyancy can lead to the formation of a gas film when it forces bubbles onto the plate surface (as in the configuration used in the present experiments). This latter condition occurs at flow speeds where the buoyancy forces dominate the motion of the gas bubbles. At higher speeds, fluctuating lift and drag forces on the individual gas bubbles can overcome buoyancy, and the process of turbulent diffusion and mixing dominates.

An examination of the relevant force ratios on individual bubbles can aid the understanding of the void-fraction stratification process. The equation of motion for a single bubble can be determined through a force balance (Maxey & Riley 1983, Magnaudet & Eames 2000). The force-ratios buoyancy-to-drag, F_B/F_D, and buoyancy-to-lift, F_B/F_L, that a bubble of radius R experiences in the near-wall shear flow are given approximately by

$$\frac{F_B}{F_D} \approx \frac{R^2 g}{9\nu(\bar{v}_f - v_b)}, \tag{4.1}$$

$$\frac{F_B}{F_L} \approx \frac{2g}{(\bar{u}_f - u_b)(\partial \bar{u}_f/\partial y)}, \tag{4.2}$$

for motion in the wall-normal y-direction. Here, the lift force on the bubble is related to the mean liquid shear, $\partial\bar{u}/\partial y$, and the lift and drag forces are related to the relative velocity between the liquid and the bubble in the streamwise, $\bar{u}_f - u_B$, and wall-normal, $\bar{v}_f - v_B$, directions. Equation (4.1) shows that the effect of buoyancy will be reduced when the bubbles are very small. In the near-wall region, the mean shear can be estimated from: $\partial\bar{u}_f/\partial y \approx u^*/\kappa y$, where κ is the von Kármán constant, and for bubbles very near the surface $y \approx R$. In addition, the relative velocity of the bubble is expected to scale with the square root of the streamwise velocity fluctuation variance; thus: $\bar{u}_f - u_B \sim \sqrt{\overline{u'^2}} \sim u^*$. Then, (4.2) becomes

$$\frac{F_B}{F_L} \approx \frac{2g}{(u^*)^2/\kappa R}. \tag{4.3}$$

For $10^{-1} < u^* < 1\,\mathrm{m\,s^{-1}}$ and $100\,\mu\mathrm{m} < R < 1\,\mathrm{mm}$, (4.3) implies $10^{-3} < |F_B/F_L| < 1$. Hence, buoyancy should play an important role in determining bubble motions for the larger bubbles at the lower speeds, as the data suggest.

Similarly, the ratio of lift to drag forces on a bubble can be found from (4.1) and (4.2) to be approximately:

$$\frac{F_L}{F_D} \approx \frac{R^2(\bar{u}_f - u_b)(\partial \bar{u}_f/\partial y)}{18\nu(\bar{v}_f - v_b)}. \tag{4.4}$$

The presence of a mean velocity gradient in the y-direction tends to drive the bubbles away from the wall into regions of lower shear, and this process is enhanced for larger bubbles. If the two velocity differences in (4.4) scale as the square root of the streamwise and wall-normal Reynolds stresses then $(\bar{u}_f - u_b)/(\bar{v}_f - v_b) \sim \sqrt{\overline{u'^2}}/\sqrt{\overline{v'^2}} \sim 2$ or 3, then (4.4) implies that $3 < |F_L/F_D| < 500$ for the parametric ranges mentioned above with $y \approx R$. Thus, shear-induced lift forces are likely to be sufficiently strong at the higher flow speeds to produce the observed migration of bubbles from near the wall. The relative absence of near-wall bubbles observed in these experiments suggests that the lift forces on the bubbles overcame the process of the turbulent diffusion that would disperse the bubbles back into the near-wall region. The process of bubble dispersion and stratification is discussed further in Sanders (2004).

Bubble stratification is associated with the loss of drag reduction. When gas is injected, it produces a significant disturbance to the incoming single-phase boundary layer; thus, the surface immediately downstream of the injector might experience reduced shear stress if a region of flow separation developed owing to gas injection. The presence or extent of such injection-induced separation was not measured in the present experiments, but its streamwise extent may be estimated. An analogous flow is that of a separation zone on a rearward-facing step. The re-attachment length of these flows is of the order of 7 to 10 times the maximum thickness of the separated region (see Laberteaux & Ceccio 2001, for a short review). For large-scale injection, the volume flux of the gas approaches that of the liquid flux of the upstream boundary layer, and the thickness of the initial bubbly layer will depend on the gas volume flux and exit velocity. Taking this thickness to be of the order of the incoming boundary-layer thickness, it is expected that the initial separation region would exist until at least 10δ, which in the present experiments is approximately 0.2 m. The BDR effect was observed to persist up to several metres downstream of the injection location, and this suggests that the observed drag reduction was not due to the formation of a separated region downstream of the injector. However, it is likely that the injection process creates a condition of low shear stress downstream of the injector, and the presence of the bubbles delays the re-establishment of the high shear at the surface. However, once significant near-wall velocity gradients reform, the migration of the bubbles away from the surface leads to a rapid loss of drag reduction.

Once ordinary single-phase boundary-layer processes have re-established themselves, the entrainment of free-stream liquid into the growing turbulent boundary layer should lead to a dilution of the bubbly mixture. This assertion can be investigated by comparing the bubbly layer thicknesses observed in the current experiments with those of a passive scalar mixed in a turbulent boundary layer. The video images recorded through the LCC windows and the prior boundary-layer-mixing results of Wieghardt (1948) and Poreh & Cermak (1964) were used for this task. The results are shown in figure 13 and include the intermediate, transitional and final zones identified by Poreh & Cermak. Here, λ is the characteristic mixed-zone thickness defined by $c(\lambda)/C_{max} = 0.5$, where $c(y)$ is the average concentration profile of the passive scalar and $C_{max}(x)$ was the maximum time-averaged concentration at downstream location x. For the current experiments, λ was estimated as half the visual bubble-layer

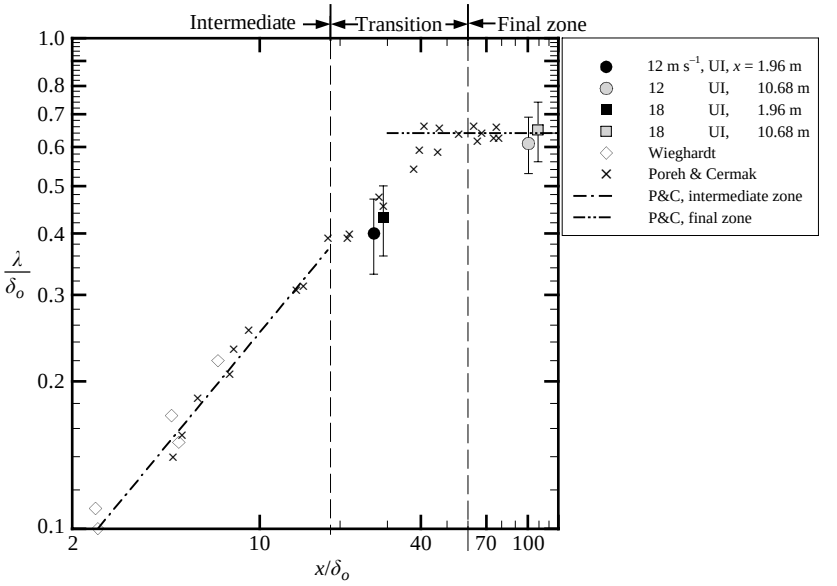

FIGURE 13. Bubble-layer thickness, λ, as a function of downstream distance; both distances are normalized by the single-phase boundary-layer thickness, δ_o. The prior data of Wieghardt (1948) and the data and fits of Poreh & Cermak (1964) are for mixing of a passive scalar in a turbulent boundary layer.

thickness and the single-phase boundary-layer thickness was used for normalization. Although bubbles are not fully passive, the results shown in figure 13 suggest that their dispersion and mixing downstream of the injector in the current experiments were similar to that of a passive scalar.

5. Summary and conclusions

The skin friction drag reduction resulting from the introduction of air bubbles into a flat-plate turbulent boundary layer has been investigated in controlled experiments at Reynolds numbers and length scales more than an order of magnitude larger than prior laboratory studies of this phenomenon. Surface shear stress was measured along with the near-wall bubble characteristics. This effort has two primary conclusions.

First, the data presented here suggest that the formation of a nearly bubble-free liquid layer next to the surface limits the amount and persistence of bubble drag reduction, and this phenomenon may be active even when buoyancy pushes bubbles toward the test surface. In the present experiments at the higher two flow speeds, this liquid layer formed within 2 m of the injector and bubble drag reduction was lost further downstream. However, the measured reductions in skin-friction drag within a metre or two of the gas injector are consistent with prior measurements at lower Reynolds numbers conducted on shorter plates.

Secondly, the amount of drag reduction strongly depends on the near-wall void fraction and the importance of bubble buoyancy. At the lowest test speed (nominally 6 m s^{-1}), the injected bubbles coalesced to form an intermittent or continuous gas film beneath the model surface, but when the free-stream speed was doubled, the injected bubbles generally remained distinct and provided friction drag reduction only as long as they remained near the surface (i.e. within 300 wall units), a result that is

consistent with the work of Pal *et al.* (1988). However, at the nominal test speeds of 12 and 18 m s^{-1}, shear-induced lift forces appear to cause bubbles to migrate from the surface, leading to the formation of the nearly bubble-free liquid layer. Simple estimates for bubble force ratios support these contentions.

In addition, the sizes and shapes of the bubbles in the near-wall flow indicate that bubble splitting is not dominant and that bubble coalescence must be more prevalent as bubbles move downstream. Additionally, the injected bubbles have diameters of the order of 100 wall units, which are larger than the smallest turbulent flow scales; however, skin-friction drag reduction was still achieved when sufficient bubbles were close to the test surface. Both of these conclusions are common to other bubble drag reduction studies. It is possible that much smaller bubbles may exhibit stronger interactions with the near-wall turbulence, and this is a topic of current study (Kawamura *et al.* 2003; Shen *et al.* 2005). Finally, the mixing and dispersion characteristics of ~100-wall-unit-diameter bubbles within a turbulent boundary layer are similar to those of a passive scalar once they are beyond the near-wall region.

The authors of this paper wish to acknowledge the significant contributions of Kent Pruss, Jinhyun Cho, Elizabeth Ivy, Paul Tortora and Hans van Sumeren of the University of Michigan; Ivo VanderHout of the Delft University of Technology; Robert Etter, Bruce Hornaday, Dr J. Michael Cutbirth, and the LCC technical staff from the Naval Surface Warfare Center – Carderock Division; and Duncan Brown of the Johns Hopkins University Applied Physics Laboratory. This effort was sponsored by the Defense Advance Research Projects Agency (Dr Lisa Porter, Program Manager) and the Office of Naval Research (Dr L. Patrick Purtell, Program Manager) under ONR contract number N00014-01-1-0880. The content of this document does not necessarily reflect the position or the policy of the United States Government, and no official endorsement should be inferred.

REFERENCES

Allen, J. M. 1977 Experimental study of error sources in skin-friction balance measurements. *J. Fluids Engng* **99**, 197–204.

Bogdevich, V. G. & Evseev, A. R. 1976 The distribution on skin friction in a turbulent boundary layer of water beyond the location of gas injection. *Investigations of Boundary Layer Control* (in Russian), Thermophysics Institute Publishing House, 62.

Bogdevich, V. G. & Malyuga, A. G. 1976 Effect of gas saturation on wall turbulence. *Investigations of Boundary Layer Control* (in Russian), Thermophysics Institute Publishing House, 49.

Bourgoyne, D. A., Hamel, J. M., Ceccio, S. L. & Dowling, D. R. 2003 Time-averaged flow over a hydrofoil at high Reynolds number. *J. Fluid Mech.* **496**, 365–404.

Chang, E. & Maxey, M. 1995 Unsteady flow about a sphere at low to moderate Reynolds number. Part 2. Accelerated motion. *J. Fluid Mech.* **303**, 133–153.

Clark III, H. & Deutsch, S. 1991 Microbubble skin friction reduction on an axisymmetric body under the influence of applied axial pressure gradients. *Phys. Fluids* A **3**, 2948–2954.

Deutsch, S. & Castano, J. 1986 Microbubble skin friction reduction on an axisymmetric body. *Phys. Fluids* **29**, 3590–3597.

Deustch, S., Moeny, M., Fontaine, A. & Petrie, H. 2003 Microbubble drag reduction in rough walled turbulent boundary layers. *Proc. ASME Fluids Engineering Division Summer Meeting 2003*, pp. 1–9.

Druzhinin, O. A. & Elghobashi, S. 1998 Direct numerical simulations of bubble-laden turbulent flows using two-fluid formulation. *Phys. Fluids* **10**, 685–697.

Etter, R. J, Cutbirth, J. M., Ceccio, S. L., Dowling, D. R. & Perlin, M. 2005 High Reynolds number experimentation in the U.S. Navy's William B. Morgan Large Cavitation Channel. *Measurement Sci. Technol.* **16**, 1701–1709.

Fernández, A., Lu, J. & Tryggvason, G. 2003 Bubble effects on wall shear in vertical flows. *Proc. ASME Fluids Engineering Division Summer Meeting 2003*, pp. 1–4.

Ferrante, A. & Elghobashi, S. 2004 On the physical mechanisms of drag reduction in a spatially developing turbulent boundary layer laden with microbubbles. *J. Fluid Mech.* **503**, 345–355.

Fontaine, A. A. & Deutsch, S. 1992 The influence of the type of gas on the reduction of skin friction drag by microbubble injection. *Exps. Fluids* **13**, 128–136.

Gowing, S. 1992 Bubble dissolving in turbulent pipe flow. *David Taylor Research Center Departmental Report*, CDNSWC/SND-1348-01.

Guin, M. M., Kato, H., Yamaguchi, H., Miyanaga, M. & Maeda, M. 1996 Direct skin friction measurements and observation of drag reduction in a two-phase air-water channel. *Proc. ASME Fluids Engineering Division Summer Meeting 1996, pp. 93–100.*

Hinze, J. O. 1955 Fundamentals of the hydrodynamic mechanism of splitting in dispersion processes. *AIChE J.* **1**, 289–295.

Hinze, J. O. 1975 *Turbulence*, 2nd edn., p. 674. McGraw-Hill.

Kawamura, T., Kakugawa, A., Kodama, Y., Moriguchi, Y. & Kato, H. 2003 Effect of bubble size on the microbubble drag reduction of a turbulent boundary layer. *Proc. ASME Fluids Engineering Division Summer Meeting 2003*, pp. 1–8.

Kodama, Y., Kakugawa, A., Takahashi, T. & Kawashima, H. 2000 Experimental study on microbubbles and their applicability to ships for skin friction reduction. *Intl J. Heat Fluid Flow* **21**, 582–588.

Laberteaux, K. R. & Ceccio, S. L. 2001 Partial cavity flows. Part 1. Cavities forming on models without spanwise variation. *J. Fluid Mech.* **431**, 1–41.

Legner, H. H. 1984 A simple model for gas bubble drag reduction. *Phys. Fluids* **27**, 2788–2790.

Lumley, J. L. 1973 Drag reduction in turbulent flow by polymer additives. *J. Polymer Sci. Macromol. Rev.* **7**, 263–290.

Lumley, J. L. 1977 Drag reduction in two phase and polymer flows. *Phys. Fluids* **20**, S64–S70.

McCormick, M. E. & Bhattacharyya, R. 1973 Drag reduction on a submersible hull by electrolysis. *Naval Engrs J.* **85**, 11–16.

Madavan, N. K., Deutsch, S. & Merkle, C. L. 1984 Reduction of turbulent skin friction by microbubbles. *Phys. Fluids* **27**, 356–363.

Madavan, N. K., Deutsch, S. & Merkle, C. L. 1985*a* Measurements of local skin friction in a microbubble-modified turbulent boundary layer. *J. Fluid Mech.* **156**, 237–256.

Madavan, N. K., Merkle, C. L. & Deutsch, S. 1985*b* Numerical investigations into the mechanisms of microbubble drag reduction. *J. Fluids Engng* **107**, 370–377.

Magnaudet, J. & Eames, I. 2000 The motion of high-Reynolds-number bubbles in inhomogeneous flows. *Annu. Rev. Fluid Mech.* **32**, 659–708.

Marié, J. L. 1987 A simple analytical formulation for microbubble drag reduction. *Physicochem. Hydrodyn.* **8**, 213–220.

Maxey, M. R. & Riley, J. J. 1983 Equation of motion for a small rigid sphere in a nonuniform flow. *Phys. Fluids* **26**, 883–889.

Meng, J. C. S. & Uhlman, J. S. 1998 Microbubble formation and splitting in a turbulent boundary layer for turbulence reduction. *Intl Symp. on Seawater Drag Reduction*, pp. 341–355.

Merkle, C. L. & Deutsch, S. 1992 Drag reduction in liquid boundary layers by gas injection. *Prog. Astronaut. Aeronaut.* **123**, 351–412.

Migirenko, G. S. & Evseev, A. R. 1974 Turbulent boundary layer with gas saturation. *Problems of Thermophysics and Physical Hydrodynamics* (in Russian).

Nagib, H., Christophorou, C., Reidi, J.-D., Monkewitz, P., Österlund, J. & Gravante, S. 2004 Can we ever rely on results from wall-bounded turbulent flows without direct measurements of wall shear stress? *AIAA Paper* 2004-2392.

Pal, S., Merkle, C. L. & Deutsch, S. 1988 Bubble characteristics and trajectories in a microbubble boundary layer. *Phys. Fluids* **31**, 744–751.

Park, J. T., Cutbirth, J. M. & Brewer, W. H. 2003 Hydrodynamic performance of the large cavitiation channel (LCC). *Proc. ASME Fluids Engineering Division Summer Meeting 2003*, pp. 1–14.

Patel V. C. 1965 Calibration of Preston tube and limitations on its use in pressure gradients. *J. Fluid Mech.* **23**, 185–208.

Pope, S. B. 2000 *Turbulent Flows*, pp. 125, 378–379. Cambridge University Press.

Poreh, M. & Cermak, J. E. 1964 Study of diffusion from a line source in a turbulent boundary layer. *Intl J. Heat Mass Transfer* **7**, 1083–1095.

Sanders, W. C. 2004 Bubble drag reduction in a flat plate boundary layer at high Reynolds numbers and large scales. Doctoral thesis, University of Michigan.

Schlichting, H. H. 1979 *Boundary Layer Theory*, 7th edn. McGraw-Hill.

Schultz-Grunow, F. 1941 New frictional resistance law for smooth plates. *NACA T M* **17**, 1–24.

Shen, X. S., Winkel, E.S., Ceccio, S. L. & Perlin, M. 2005 Influence of bubble size reduction on micro-bubble drag reduction. *Proc. FAST'2005, St Petersburg, Russia.*

Takahashi, T., Kakugawa, A., Nagaya, S., Yanagihara, T. & Kodama, Y. 2001 Mechanisms and scale effects of skin friction reduction by microbubbles. 2nd *Symp. on the Smart Control of Turbulence*, pp. 1–9.

Vance, M. W., Sugiyama, K., Takagi, S. & Squires, K. D. 2003 Microbubble transport in turbulent channel flow. *Proc. ASME Fluids Engineering Division Summer Meeting 2003*, pp. 1–8.

White, F. M. 1991 *Viscous Fluid Flow*, 2nd edn. McGraw-Hill.

Wieghardt, K. 1948 Uber Ausbreitungsvorgange in Turbulenten Reibungsschichten. *Z. Angew. Math. Mech.* **27**, 346–355.

Xu, J., Maxey, M. R. & Karniadakis, G. E. 2002 Numerical simulation of turbulent drag reduction using micro-bubbles. *J. Fluid Mech.* **468**, 271–281.

Yu, P.-W. & Ceccio, S. L. 1997 Diffusion induced bubble populations downstream of a partial cavity. *J. Fluids Engng* **119**, 732–787.